Rational design of mixed-matrix metal-organic framework membranes for molecular separations

Shuvo Jit Datta[1,2], Alvaro Mayoral[3,4,5], Narasimha Murthy Srivatsa Bettahalli[1], Prashant M. Bhatt[1,2], Madhavan Karunakaran[1]†, Ionela Daniela Carja[2], Dong Fan[6], Paulo Graziane M. Mileo[6], Rocio Semino[6], Guillaume Maurin[6], Osamu Terasaki[3,4], Mohamed Eddaoudi[1,2]*

Conventional separation technologies to separate valuable commodities are energy intensive, consuming 15% of the worldwide energy. Mixed-matrix membranes, combining processable polymers and selective adsorbents, offer the potential to deploy adsorbent distinct separation properties into processable matrix. We report the rational design and construction of a highly efficient, mixed-matrix metal-organic framework membrane based on three interlocked criteria: (i) a fluorinated metal-organic framework, AlFFIVE-1-Ni, as a molecular sieve adsorbent that selectively enhances hydrogen sulfide and carbon dioxide diffusion while excluding methane; (ii) tailoring crystal morphology into nanosheets with maximally exposed (001) facets; and (iii) in-plane alignment of (001) nanosheets in polymer matrix and attainment of [001]-oriented membrane. The membrane demonstrated exceptionally high hydrogen sulfide and carbon dioxide separation from natural gas under practical working conditions. This approach offers great potential to translate other key adsorbents into processable matrix.

C hemical separations are highly energy intensive and account for about half of the global industrial energy consumption (1, 2). Membrane-based separation can provide an energy-efficient alternative to traditional separation processes such as cryogenic distillation and adsorptive separation. Polymer membranes intrinsically undergo a trade-off between the permeability (productivity) and selectivity (efficiency), which is known as Robeson's upper bound (3, 4). Mixed-matrix membranes (MMMs), which combine the distinct properties of selective adsorbents (molecular separation and facilitated gas transport) and polymers (processability and mechanical stability), may enable energy-efficient and environmentally sustainable technologies (5–7). Nevertheless, successful translation of adsorbent distinct properties into MMMs remains a persistant challenge because of recurring agglomeration and sedimentation of adsorbent fillers in the polymer matrix and incompatibility between adsorbent-polymer interfaces. As a result of these challenges, the attainment of highly selective membranes is hampered and the mechanical properties of the membranes are lessened (8).

Various MMMs using isotropic or near-anisotropic fillers have been reported (6, 7, 9), and these membranes exhibited moderate improvement in selectivity and/or permeability (7, 10, 11). The impact of filler particle size (12), morphology (6, 13), functionality (14), and surface modification (15) in MMMs on gas separation is well documented. An anisotropic morphology, such as high-aspect-ratio nanosheets, was recognized to offer several advantages over isotropic fillers. The relatively large external surface area proffers an enhancement of nanosheet-polymer interface compatibility, permitting high filler loading, and the combination of very short gas diffusion pathways with preserved molecular discrimination may result in a considerable increase of both permeability and selectivity (16).

Only a limited number of metal–organic framework (MOF) nanosheets have been explored in MMMs for gas separation (17–22). Cu-BDC nanosheets [from two-dimensional (2D) layer-structured MOF] were first embedded in Matrimid polymer in a form of MMM for CO_2/CH_4 separation (17). The membrane showed moderate selectivity improvement at the expense of a lower CO_2 permeability, plausibly because of nonselective nor promoting transport of CO_2 versus CH_4 in the relatively larger pore system (~6.5 Å). NH_2-MIL-53(Al), a 3D periodic framework with relatively strong CO_2 interactions, was prepared as nanosheets using cetyltrimethyl ammonium bromide (CTAB) surfactant (18). Unfortunately, the resultant MMM showed a relatively moderate CO_2/CH_4 separation, possibly because residual CTAB on the surface of nanosheets affected the gas

separation properties of the pristine material, pinpointing the importance of surfactant-free nanosheet preparation. Methods to use contracted pore and/or better-performing MOF structures as defect-free nanosheets is of prime importance, because numerous contracted pore MOF structures offer desirable adsorption and molecular diffusion properties (23) but are not ideal for conventional exfoliation methods (24). In addition to the attainment of high-aspect-ratio nanosheets of the desired MOFs, it is essential to develop suitable strategies that can afford requisite alignment of nanosheets within the polymer matrix.

We report a concept for the construction of a mixed-matrix MOF (MMMOF) membrane based on three interlocked criteria: (i) a MOF filler with optimal pore size and shape, functionality, and a host-guest interaction that selectively enhances H_2S and CO_2 diffusion while excluding CH_4; (ii) tailoring MOF crystal morphology along the 001 crystallographic direction into high-aspect-ratio (001) nanosheets that proffer maximum exposure of 1D channel and promote a nanosheet-polymer interaction resulting in high nanosheet loading; and (iii) in-plane (face-to-face) alignment of (001) nanosheets in a polymer matrix with proximal distance to translate the molecular separation properties of single nanosheets into a uniformly [001]-oriented macroscopic MMMOF membrane.

Hydrolytically stable fluorinated AlFFIVE-1-Ni (KAUST-8), when used as an adsorbent, showed excellent separation properties for H_2S/CH_4 and CO_2/CH_4 (25, 26). This MOF has appropriate H_2S and CO_2 adsorption and separation properties and high chemical stability toward H_2S that instigate AlFFIVE-1-Ni as a potential molecular sieve filler in MMMOF membrane for natural gas upgrading. However, effective deployment of AlFFIVE-1-Ni (a three-periodic MOF with 1D channels) as a filler into membranes requires its morphology to be tailored into nanosheets with defined crystallographic direction for maximum surface exposure of 1D channels (25, 26).

The structure of AlFFIVE-1-Ni along the [110] or [1-10] direction is shown in Fig. 1A. The two-periodic square-grid layer constructed by linking Ni(II) with pyrazine ligand is pillared by $[AlF_5(H_2O)]^{2-}$ anions in the third dimension to construct a three-periodic framework/structure with the primitive cubic (pcu) underlying topology and pore walls composed of $[AlF_5(H_2O)]^{2-}$ anions, prohibiting access to the pore system in the [110] or [1-10] direction (Fig. 1A). Schematic illustrations of a typical truncated-bipyramidal morphology of the crystal and its channel orientation are shown in Fig. 1B. The structure consists of 1D ultrasmall channels (represented in green) that run along the [001] direction (Fig. 1, B and C). These channels are

[1]Division of Physical Science and Engineering, Advanced Membrane and Porous Materials Center, King Abdullah University of Science and Technology (KAUST), Thuwal 23955-6900, Kingdom of Saudi Arabia. [2]Division of Physical Science and Engineering, Advanced Membrane and Porous Materials Center, Functional Materials Design, Discovery and Development (FMD[3]), KAUST, Thuwal 23955-6900, Kingdom of Saudi Arabia. [3]Centre for High-Resolution Electron Microscopy, School of Physical Science and Technology, ShanghaiTech University, Shanghai 201210, China. [4]Shanghai Key Laboratory of High-Resolution Electron Microscopy, ShanghaiTech University, Shanghai 201210, China. [5]Instituto de Nanociencia y Materiales de Aragon, CSIC – Universidad de Zaragoza, Laboratorio de Microscopias Avanzadas, 50009 Zaragoza, Spain. [6]Institut Charles Gerhardt Montpellier (ICGM), University of Montpellier, CNRS, ENSCM, 34095 Montpellier, France.
*Corresponding author. Email: mohamed.eddaoudi@kaust.edu.sa
†Present address: Centre for Carbon Fiber and Prepregs, Council of Scientific and Industrial Research (CSIR), National Aerospace Laboratories, Bengaluru 560017, India.
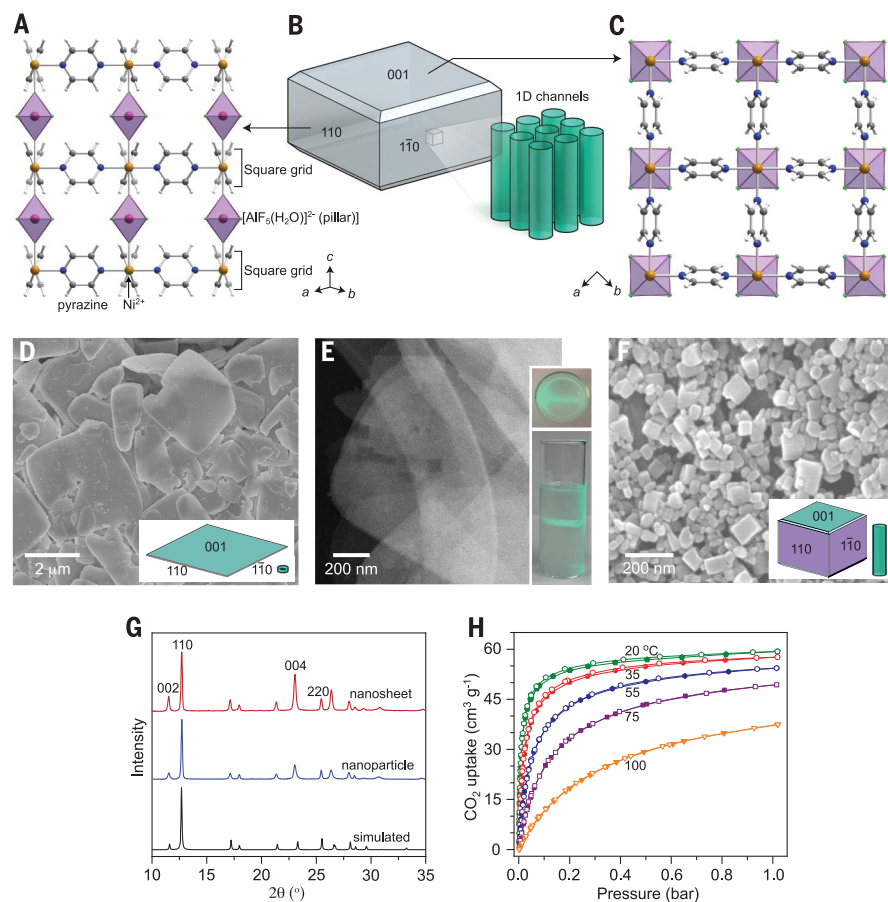
Fig. 1. Crystal structure and morphology of AlFFIVE-1-Ni (point group 4/mmm). (**A**) Structure view along the [110] or [1-10] direction. (**B**) Schematic illustration of truncated bipyramidal morphology and 1D channel orientation. (**C**) Structure view along the [001] direction. (**D**) SEM image of nanosheets. Inset: large 001 surface and short channel. (**E**) Low-resolution STEM image of nanosheets. Inset: photos showing Tyndall effect on nanosheets using a green laser. (**F**) SEM image of nanoparticles. Inset: depicted crystal morphology and long channel. (**G**) XRD patterns (λ = 1.54056 Å) of nanosheets and nanoparticles. (**H**) CO_2 adsorption isotherms of nanosheets between 20 and 100°C.

accessible to only relatively small gas molecules (e.g., He, H_2, CO_2, O_2, H_2S, N_2, etc.).

Synthesis and characterization of MOF nanosheets

A scanning electron microscopy (SEM) image of AlFFIVE-1-Ni crystals, obtained by conventional hydrothermal synthesis, corroborates that the material is not suitable for membrane fabrication (fig. S1). Grinding large particles into nanoparticles may not improve their gas separation performances because most of the nanoparticles may expose the nonaccessible (110) and (1-10) facets. The 1D channels of AlFFIVE-1-Ni can only be fully exploited if the morphology is controlled into nanosheets with completely exposed (001) facet. Therefore, the crystallographic growth along the c direction must be substantially reduced or completely suppressed relative to the desired growth along the a and b directions. We developed a bottom-up synthesis approach yielding high-aspect-ratio nanosheets. Performing the synthesis under a reduced $[AlF_5(H_2O)]^{2-}$ pillaring unit concentration, along with decreasing synthesis temperature, promoted the formation of crystals with large lateral dimensions and prevented growth in the c direction (Fig. 1A, supplementary materials, and figs. S1 and S2). Further, the addition of ethanol into the reaction mixture was found to be very effective at further reducing crystal thickness while maintaining the nanosheet morphology (fig. S3).

Diverse MOF nanosheets have been prepared either from 2D layer-structured MOFs by exfoliation methods (27), or from a 3D periodic framework by the 2D oxide sacrifice approach (28), and/or using surfactant-assisted synthesis (18, 29). We present a bottom-up synthesis method for the preparation of MOF nanosheet from a 3D periodic fluorinated MOF with a contracted pore system (25). We did not use surfactant, modulator, or template, and synthesis was accomplished at a relatively low temperature (55°C). The resultant nanosheets are defect-free (STEM analyses) and undesirable substance free, the essential requirements for membrane application. The optimized synthesis method differs from bulk synthesis (25) and is scalable (fig. S4).

Adjusting the synthesis conditions afforded the crystal morphology control from aggregated truncated bipyramidal morphology to nanosheets (Fig. 1D and figs. S1 to S3). SEM images revealed that synthesized square-shaped nanosheets exhibited an average lateral dimension of 0.5 to 4 μm and thickness in the range of 20 to 50 nm, resulting in an aspect ratio >25 (Fig. 1D). A scanning transmission electron microscopy (STEM) image of nanosheets (Fig. 1E) corroborated the higher aspect ratio. The nanosheet dispersion is supported by the observed Tyndall effect using a green laser (Fig. 1E, inset, and movie S1). The X-ray diffraction (XRD) pattern of the material (Fig. 1G) shows preferred orientation effect of (001) nanosheets with the 00l (l = 2n) reflections significantly enhanced, further confirming the successful synthesis of nanosheets with AlFFIVE-1-Ni structure.

In addition, we developed a synthesis method to produce nanoparticles (Fig. 1F). The SEM image revealed that nanoparticles were fairly uniform with particle size of ~50 to 120 nm, and XRD confirmed the AlFFIVE-1-Ni structure (Fig. 1G). The CO_2 sorption isotherms affirmed that bulk material, nanosheets, and nanoparticles exhibited similar CO_2 uptake capacity (fig. S5). Variable temperature CO_2 adsorption isotherms on nanosheets are shown in Fig. 1H. The versatility and scope of our MOF nanosheet synthetic strategy was further evaluated with the fabrication of the FeFFIVE-1-Ni (KAUST-9) nanosheets (fig. S6) (25).

Atomic structure analysis of MOF nanosheets

Annular bright-field (ABF) images taken with the C_s-corrected STEM from the nanosheet along the [001] and the [100] directions are shown in Fig. 2, A and D, respectively. The images offer an unambiguous visualization of the atomic structure. The corresponding Fourier diffractogram and selected area electron diffraction pattern were inserted at the top right in the images, with indices based on the space group $I4/mcm$ with a = 9.86 Å and c = 15.25 Å. The image resolution was confirmed to be 1.6 Å by 0 to 60 reflection marked by a red circle in the Fourier diffractogram of Fig. 2A, and was among the highest spatial resolutions ever achieved for any MOFs. This observation (and figs. S7 and S8) corroborates the preferential crystal orientation of (001)-AlFFIVE-1-Ni nanosheets. A symmetry-averaged image (Fig. 2A) with p4mmm improved signal-to-noise ratio greatly and specified the atoms (Fig. 2B). Strong dark spots were observed with
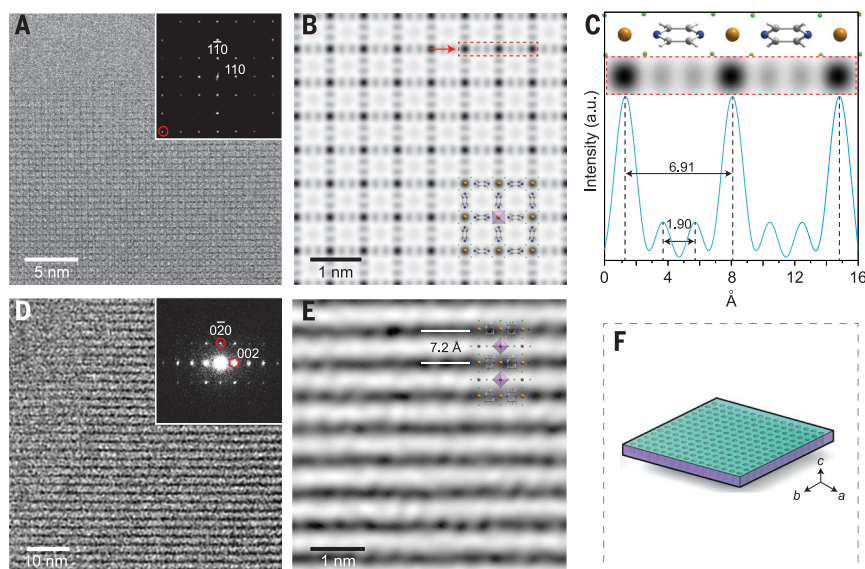
Fig. 2. C_s-corrected STEM images of AlFFIVE-1-Ni nanosheets acquired from different zone axes. (**A**) ABF image along [001] with the Fourier diffractogram (FD). (**B**) Symmetry-averaged image of (A) and an overlaid crystal structure. (**C**) Enlarged a part marked by the dotted red rectangle and intensity profile along the red arrow of (B) and the associated structure model. (**D**) ABF image taken with [100] incidence. (**E**) Wiener-filtered image with superimposed atomic structure. Orange indicates Ni(II); purple, Al(III); gray, carbon; green, fluorine; and blue, nitrogen. (**F**) Schematic illustration of nanosheet with 1D channel orientation.

separation of ≈6.91 Å, consistent with the distance between adjacent inorganic extended chains (columns) formed by –F–Ni–F–Al–F– (Fig. 2C). Additionally, two weak, dark elongated signals were also observed between the strong dark spots (separated by ≈1.9 Å), which can be attributed to a part of pyrazine, two carbon atoms, and one nitrogen atom, acting as a linker between adjacent Ni(II).

Overcoming a big difficulty induced by the preferred orientation of nanosheets along the [001], high-resolution ABF images were taken with the [100] incidence, which is perpendicular to the [001] direction (Fig. 2D and fig. S9). Figure 2D visualizes the square grid of Ni(II) and pyrazine pillared by $[AlF_5(H_2O)]^{2-}$, where the dark contrast is associated with Ni(II). The crystal structure of AlFFIVE-1-Ni along the [100] direction matches well the corresponding experimental ABF image (Fig. 2E and fig. S9). This in-depth STEM study confirms the successful synthesis of (001)-AlFFIVE-1-Ni nanosheets [hereafter referred to as (001)-AlFFIVE or (001) nanosheets] with excellent crystallinity and maximum exposure of 1D channels (Fig. 2F), which is a highly desirable morphology for achieving in-plane alignment of nanosheets in the polymer matrix.

Fabrication of [001]-oriented MMMOF membrane

It is of prime importance to in-plane align (001) nanosheets in a polymer matrix to fabricate a uniform [001] oriented/c-oriented MMMOF membrane and translate the 1D channel alignment from single nanosheets into a macroscopic continuous membrane for an efficient molecular separation (Fig. 3A). Commercially available state-of-the-art polyimide 6FDA-DAM, and laboratory-synthesized 6FDA-DAM-DAT (1:1) and 6FDA-DAT polyimides were chosen as polymer matrices because of their high thermal and chemical stabilities, good mechanical strength, and excellent processability. We examined three different solvents, chloroform ($CHCl_3$), tetrahydrofuran (THF), and dichloromethane (DCM), as dispersant media to evaluate the effect of solvents for membrane fabrication and resultant CO_2/CH_4 separation. A solution-casting method was performed to fabricate pure polymeric and MMMOF membranes with a thickness of ~50 to 70 μm (see the supplementary materials and methods). The solvent effect in pure polymeric membranes was minimal. However, in MMMOF membrane, $CHCl_3$ presented higher CO_2/CH_4 selectivity followed by THF and DCM (figs. S10 and S11 and table S1). We evaluated the nanosheets' dispersibility in different solvents and allowed them to sediment. The nanosheets began sedimentation after ~6 to 8 hours in DCM and after ~22 to 25 hours in THF, and there was no sedimentation in $CHCl_3$ even after 5 days. Thus, higher selectivity can be attributed to the better nanosheet dispersibility that prevents nanosheet sedimentation and/or agglomeration during membrane fabrication, resulting in homogeneous nanosheet alignment inside the polymer matrix.

The cross-section SEM images of 58.9 wt % nanosheets in 6FDA-DAM [(001)-AlFFIVE(58.9)/ 6FDA-DAM, with the parentheses referring to MOF loading by wt %] reveal a uniform in-plane alignment of nanosheets in the polymer matrix (Fig. 3B and fig. S12). The focused ion beam SEM images on an extensive area show that most of the nanosheets were uniformly and in-plane aligned throughout the membrane (Fig. 3C, fig. S13, and movie S2). These analyses also revealed an excellent nanosheet-polymer interface compatibility. XRD patterns of associated membrane (Fig. 3D) show only two major Bragg diffractions [indexed as the (002) and (004) crystallographic planes of AlFFIVE-1-Ni structure], corroborating the strong preferential in-plane alignment of (001) nanosheets and the attainment of the desired uniform [001]-oriented MMMOF continuous membrane. These results demonstrate that the successful translation of single (001) nanosheets into a [001]-oriented macroscopic membrane, where 1D channels of nanosheets are all parallel, an ideal scenario for distinct molecular separation (Fig. 3A).

Shear flow– or shear force–induced preferential alignment of 2D nanosheets within polymer matrix have been reported (*17, 30*). Here, (001) nanosheet in-plane (*c* axis) alignment was induced by a slow evaporation of solvent "slow evaporation-induced in-plane alignment of nanosheets" in the course of the membrane fabrication process. During slow solvent evaporation, nanosheets gradually self-arrange according to the minimum energy configuration (*31*). The nanosheet concentration gradient and presence of the liquid-vapor interface may assist as a nucleating surface, causing in-plane–aligned nanosheet domains to grow gradually inward (Fig. 3E). If the solvent evaporation process is relatively fast, then the nanosheet alignment may be kinetically affected, and the final alignment may consolidate into a thermodynamically unfavored state (Fig. 3G) (*32*). In addition, a solvent/(nanosheet+polymer) mass ratio of 22 to 35 was found to be an optimal range for suitable in-plane alignment. Centrifugal force can also align nanosheets; therefore, [001]-oriented ultrathin membrane on a porous α-Al_2O_3 support was prepared with a spin-coating method.

MOF loading, and associated properties of membranes, were additionally analyzed by thermogravimetric analysis, Fourier transform infrared spectroscopy, and XRD (figs. S14 to S16). We attained nanosheets loadings up to 59.8 wt % in 6FDA-DAM-DAT and 60.3 wt % in 6FDA-DAT, loadings (up to 60 wt %) that are substantially higher than isotropic filler loadings (<35 wt %) (*10*). The ability to increase nanosheet loading offers an opportunity to closely mimic the associated pure MOF membrane, as well as to improve the separation performance of the membranes
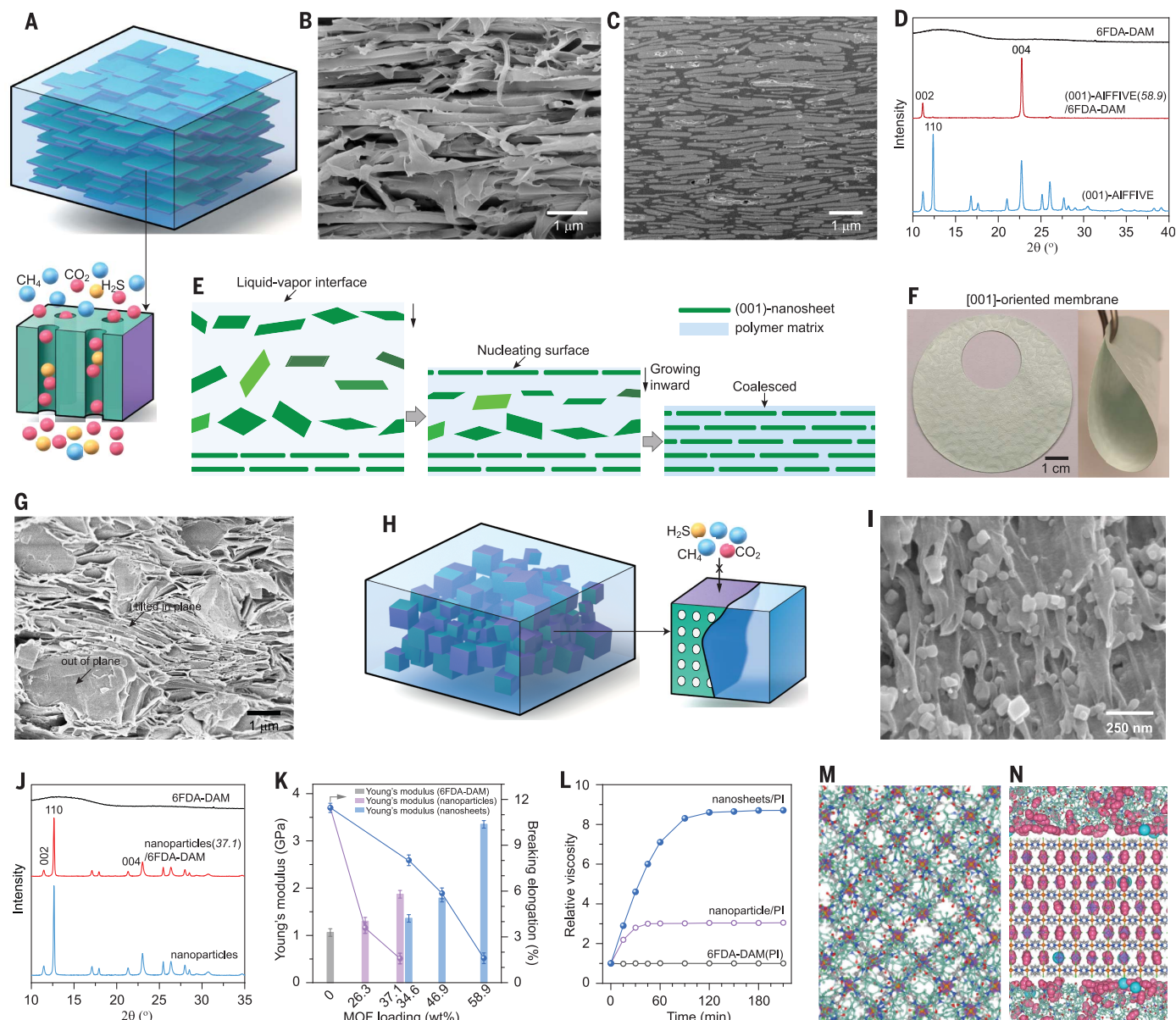
Fig. 3. Fabrication and characterization of [001]-oriented MMMOF membranes.
(**A**) Schematic illustration of [001]-oriented membrane and an efficient H_2S and CO_2 separation process through 1D channel. (**B** and **C**) Cross-section SEM image (B) and focused ion beam-SEM image (C) of (001)-AlFFIVE(58.9)/6FDA-DAM membrane. (**D**) XRD patterns of [001]-oriented membrane and nanosheet crystallite. (**E**) Illustration of "slow evaporation-induced in-plane alignment" of nanosheets in polymer matrix. (**F**) Photographs of membrane. (**G**) Cross-section SEM image of random fashion nanosheet membrane. (**H**) Illustration of random fashion nanoparticles embedded in polymer matrix. (**I** and **J**) Cross-section SEM image (I) and XRD pattern (J) of nanoparticle(37.1)/6FDA-DAM membrane. (**K**) Mechanical studies of the membranes. (**L**) Relative viscosity changes of MOF/polymer and polymer suspension. (**M** and **N**) Computational studies of [001]-oriented membrane. Blue, polymer phase; green, MOF in (001) facet; purple, MOF in (110) or (1-10) facet.

because the agglomeration, sedimentation, and random orientation of nanosheets within the polymer matrix is circumvented at high loadings. In the present case, no such adverse effects were observed (figs. S17 to S20).

Schematic illustrations of randomly oriented AlFFIVE-1-Ni nanoparticles embedded in polymer matrix are shown in Fig. 3H. The cross-section SEM image and XRD pattern of 37.1 wt % nanoparticles in 6FDA-DAM polymer showed a random orientation of the nanoparticles inside polymer matrix (Fig. 3, I and J, and fig. S21). Young's modulus and elongation strain of nanoparticles and nanosheets containing membranes were evaluated (Fig. 3K and fig. S22). It was found that the incorporation of nanoparticles or nanosheets into polymer matrix results in an enhancement of Young's modulus, and this enhancement was substantial in nanosheets containing membranes (Fig. 3K and table S3), which can be attributed to the better compatibility between nanosheets and polymer. Membranes fabricated using nanoparticles maintain good mechanical properties at relatively low MOF loading (26.3 wt %). Nanoparticle loadings up to 37.1 wt % were possible before the membrane became defective or too fragile to handle for gas separation studies. High loading (up to 58.9 wt %) was possible using nanosheets (Fig. 3K and
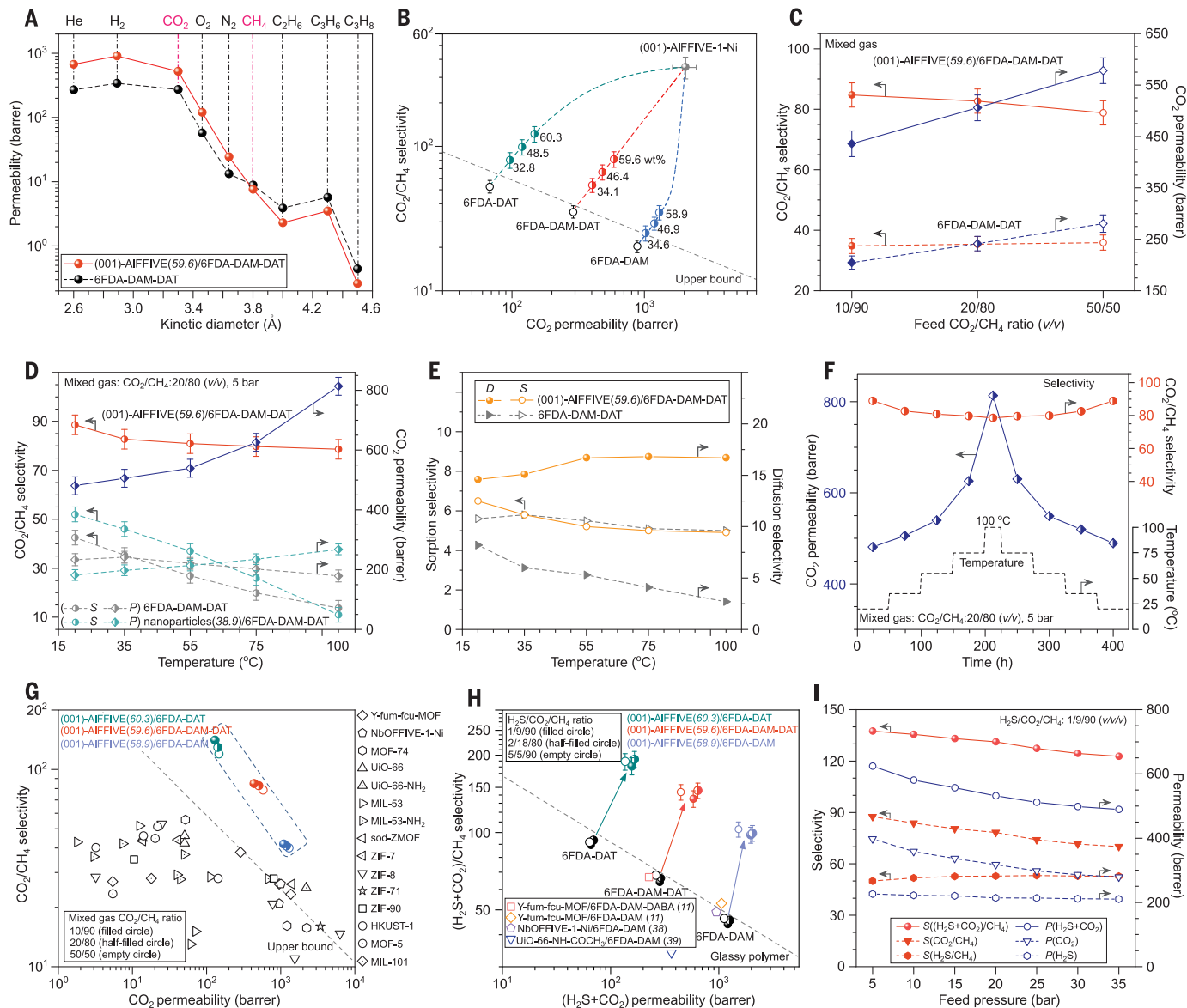
Fig. 4. Gas separation properties. (A) Gas permeability of gases with various kinetic diameters. **(B)** CO_2 permeability and CO_2/CH_4 selectivity of [001]-oriented MMMOF membranes with various nanosheets loading in wt % and predicted pure (001)-AlFFIVE-1-Ni membrane with pure gas permeation (CO_2 at 1 bar and CH_4 at 4 bar, 35°C). **(C** and **D)** Effects of feed CO_2 concentration and temperature on CO_2 permeability and CO_2/CH_4 selectivity for [001]-oriented and pure polymeric membranes with mixed-gas permeation (CO_2/CH_4: 50/50 at 2 bar, 20/80 at 5 bar, and 10/90 at 10 bar, 35°C) (C) and temperature between 20 and 100°C (D). **(E)** Variation of CO_2/CH_4 sorption and diffusion selectivity with respect to temperature between 20 and 100°C. **(F)** Long-term stability and reversibility of CO_2 permeability and CO_2/CH_4 selectivity under thermal stress in (001)-AlFFIVE(59.6)/6FDA-DAM-DAT membrane. **(G)** Plot of

CO_2/CH_4 selectivity versus CO_2 permeability from a recent literature review of polymer/MOF-based MMMs (table S15). **(H)** (H_2S+CO_2)/CH_4 mixed-gas separation properties of [001]-oriented and pure polymer membranes and comparison with the literature; permeation conditions and individual H_2S and CO_2 permeability and H_2S/CH_4 and CO_2/CH_4 selectivity are listed in table S16. The dashed black line indicates the general trade-off between permeability and selectivity in glassy polymers under the described test conditions. **(I)** Permeability and selectivity of [001]-oriented membrane under feed pressures between 5 and 35 bar at 35°C. The dashed black line in (B) and (G) indicates the Robeson upper bound for state-of-the-art polymer membranes (3). The average permeation data are presented; error bars represent the SE of three membranes (n = 3). 1 barrer = 10^{-10} cm$^3_{STP}$ cm cm^{-2} s^{-1} cmHg^{-1}.

fig. S22). Nanosheets proffered smooth and extended external surface area compared with nanoparticles, which promoted interactions with the polymer. The optimum nanosheet loading was found to be up to 64 wt %. Beyond this limit, the resultant membrane was difficult to handle for gas separation studies because of its apparent fragility

and plausible defects, resulting in relatively high permeability with lower selectivity.

We further endeavored to elucidate the enhanced interaction between nanosheets and polymer. The MOF-polymer suspension was prepared by stirring (250 rpm) at 35°C for 2 hours before membrane casting. The MOF-polymer suspension became viscous and the

relative viscosity change of the nanosheet-polymer suspension was considerably higher than that of nanoparticle-polymer suspension (Fig. 3L). The higher viscosity of the suspension implies an enhanced nanosheet-polymer interaction. It is possible that the hydrogen-bonding interaction between the imide groups of the 6FDA and the H of the pyrazine from

(001) nanosheets provides better mechanical properties of nanosheet-incorporated membranes.

The gas separation performances of nanoparticles and (001) nanosheet–containing membranes were assessed under an equimolar CO_2/CH_4 mixture and compared based on the volume and weight fraction (fig. S23). The nanosheet membranes demonstrated substantially better separation. Even at similar MOF loading, nanosheets offered higher permeability and selectivity (fig. S23). Nanoparticles always compensate permeability to gain selectivity that can be attributed to random orientation of nanoparticles with nonpermeable (110) and (1-10) facets perpendicular to gas diffusion direction (Fig. 3I), ascertaining the importance of (001) nanosheet morphology.

We also fabricated membrane using (001) nanosheets in a randomly aligned fashion and evaluated CO_2/CH_4 separation (fig. S24). The membrane presented high permeability but significantly reduced selectivity, presumably because of the presence of a nonselective gas diffusion path associated with discontinuity of nanosheet staking, as revealed by SEM images (Fig. 3G and fig. S24AB). This comparative study corroborates that in-plane alignment is essential to maximizing membrane performance (fig. S24C).

We further evaluated how pore size and shape and host-guest interactions are critical for concurrent enhancement of selectivity and permeability. Accordingly, we selected three MOFs with nanosheet morphology and with different pore system features. Ultra-small-pore (~2.1 Å), $Zn_2(bim)_4$ nanosheets showed a negligible improvement in the selectivity associated with a substantial decrease in permeability. Relatively large pore (~6.2 Å), Zn-TCPP nanosheets showed higher permeability but were associated with reduced selectivity (fig. S25). These results are consistent with CO_2 adsorption isotherms of associated MOF nanosheets (fig. S25). Only (001)-AlFFIVE nanosheets MMMOF demonstrated a significant concurrent enhancement of selectivity and permeability.

The in silico–constructed (001)-AlFFIVE/polymer composite model is illustrated in Fig. 3M and figs. S27 to S30. The top views show that polymer covers 1D channel of (001) nanosheets (Fig. 3M), forming interlocked perpendicular pore zones. The side views confirm that the polymer remains at the MOF surface, so there is no polymer penetration into the pores (fig. S27). We constructed a second nanosheet/6FDA-DAM composite model corresponding to a 42 wt % (001) nanosheet loading in complement to the pristine one associated with a 59 wt % (001) nanosheet loading (fig. S27). The association of two components in the interfacial region is held by means of continued hydrogen-bonding interactions with a nanosheet-polymer interface distances that ranged from 2.5 to 6.5 Å for both membranes (fig. S27, C and F). The so-created interfacial region is characterized by the presence of interconnected pores from 2.5 to 4.0 Å (fig. S29). This restricted dimension a priori prevents the gas from spreading along the direction parallel to the nanosheets surface, thus favoring straight-forward pathways for the gas through the oriented 1D channel nanosheets/polymer, pinpointing the importance of uniform [001]-oriented membranes for enhanced separation performance. Grand canonical Monte Carlo (GCMC) simulations were performed to assess the CO_2 and CH_4 separation properties of the resulting membranes at 298 K. Analysis of single-component (fig. S31) and binary mixture (Fig. 3N and fig. S31C) adsorption studies support the adsorption of CH_4 exclusively in the polymer phase while CO_2 equally populates the pores of the MOF and polymers (Fig. 3N and fig. S31), confirming that nanosheets act as a molecular barrier for CH_4. The interfacial region was found to be accessible to gas molecules, thus ensuring a connecting path between the polymer and the oriented 1D MOF channel.

Impact of three interlocked criteria on gas separation properties

We conducted single-gas permeation on [001]-oriented membranes and associated polymer membranes using nine different gas molecules (fig. S32 and table S4). The [001]-oriented membranes showed higher CO_2 permeability compared with pure polymer membranes, and their CH_4 permeability remained similar (Fig. 4A). This result corroborates a more effective transport of CO_2 through 1D channels of (001) nanosheets that leads to enhanced CO_2/CH_4 selectivity. This is a highly sought-after property in a MOF filler because it allows its deployment with various polymer matrices for concurrent enhancement of selectivity and permeability (fig. S32 and table S4).

Theoretical CO_2/CH_4 selectivity and CO_2 permeability of pure (001)-AlFFIVE-1-Ni membrane were 354 and 2035 barrer (back-calculated using Maxwell model). Experimentally obtained CO_2 permeability and CO_2/CH_4 selectivity of (001)-AlFFIVE/6FDA-DAM, (001)-AlFFIVE/6FDA-DAM-DAT, and (001)-AlFFIVE/6FDA-DAT membranes at different nanosheets loading are shown in Fig. 4B and table S5. The in-plane–aligned incorporation of nanosheets into the polymer matrix prompted a substantial increase in both CO_2 permeability and CO_2/CH_4 selectivity (Fig. 4B and table S5).

Single and mixed-gas separation studies under different CO_2 feed compositions (CO_2/CH_4: 10/90; 20/80 and 50/50) and feed pressure on [001]-oriented membranes and associated pure polymer membranes are shown in Fig. 4C and figs. S33 to S35. The (001)-AlFFIVE/6FDA-DAM membrane exhibited a higher CO_2/CH_4 selectivity under mixed-gas feeds compared with single-gas feeds, in contrast to pure 6FDA-DAM (fig. S33B). Under mixed-gas permeation, the preferential adsorption of CO_2 in nanosheets led to substantially reduced CH_4 permeability and thus enhanced CO_2/CH_4 selectivity (fig. S33D). The (001)-AlFFIVE/6FDA-DAM-DAT and (001)-AlFFIVE/6FDA-DAT membranes presented similar single- and mixed-gas selectivity (figs. S34D and S35D).

A CO_2 concentration–dependent study revealed that mixed-gas CO_2 permeability was similar to that of single-gas permeability at a relatively high-feed CO_2 concentration (CO_2/CH_4:50/50); nevertheless, CO_2 permeability gradually decreased as CO_2 feed concentration decreased to CO_2/CH_4: 20/80 to 10/90 while selectivity was preserved (figs. S33D, S34D, and S35D). This CO_2 permeability decrease is highly likely because of the higher competition between CH_4 and CO_2. These results imply that CO_2/CH_4 separation at relatively low CO_2 concentration (CO_2/CH_4:20/80 and 10/90, typical CO_2 concentration in natural gas) is challenging but is of practical importance. Even under CO_2/CH_4:10/90 mixture, mixed-gas CO_2 permeability improvements of 113% and 110% and CO_2/CH_4 selectivity enhancements of 144% and 139% were achieved for (001)-AlFFIVE(59.6)/6FDA-DAM-DAT and (001)-AlFFIVE(60.3)/6FDA-DAT membranes, respectively, compared with associated pure polymer membranes (Fig. 3C, figs. S34 and S35, and tables S7 and S8). The enhanced separation corroborates the importance of judicious choice of MOF fillers and polymer pairs. These results also demonstrate that the relative enhancement of permeability and selectivity is pronounced in relatively low-permeable polymer (tables S6 to S8).

Temperature-dependent (20 to 100°C) single- and mixed-gas CO_2/CH_4 separation on [001]-oriented membranes and associated pure polymer membranes are shown in Fig. 4D and figs. S36 to S38. Increasing the permeation temperature significantly affects the CO_2/CH_4 separation. Particularly, both selectivity and permeability of pure polymeric membranes and the membrane with embedded nanoparticles substantially deteriorated (Fig. 3D and figs. S36 to S38). By contrast, in [001]-oriented membranes, the CO_2 permeability significantly increased with increasing temperature while retaining selectivity (figs. S37 and S38). We also obtained variable-temperature CO_2 adsorption isotherms on (001) nanosheet powder (Fig. 1H). As the temperature increased, the CO_2 adsorption decreased (weaker interactions). This decrease was pronounced for a temperature increase from 75 to 100°C, prompting a significant enhancement of CO_2 permeability at relatively higher temperatures (figs. S36 to S38). The (001)-AlFFIVE/6FDA-DAM-DAT membrane demonstrated a marked concurrent enhancement

in CO_2 permeability of 355% and CO_2/CH_4 selectivity of 470% compared with the pure 6FDA-DAM-DAT polymer, even at 100°C and under (CO_2/CH_4: 20/80) separation (Fig. 4D and tables S9 to S11). This CO_2/CH_4 separation at elevated temperature is the consequence of enhanced CO_2 diffusion through 1D channels of (001) nanosheets, uniform in-plane alignment of nanosheets, and substantially high nanosheet loading.

We deconvoluted CO_2 and CH_4 permeability into diffusion coefficient (diffusivity, D_i) and sorption coefficient (solubility, S_i) based on the solution-diffusion model (33). By changing the permeation temperature, the membranes exhibited opposite propensy of solubility and diffusivity of the gases (CO_2 and CH_4). Specifically, increasing the temperature considerably decreased CO_2 and CH_4 solubility but substantially increased CO_2 diffusivity in both membranes (fig. S39, A and B). The (001)-AlFFIVE/6FDA-DAM-DAT membrane demonstrated a significant enhancement in CO_2 diffusivity but a sharp decrease in CH_4 diffusivity compared with 6FDA-DAM-DAT (fig. S39, A and B, and table S12), affording a diffusion dominated with exceptionally high CO_2/CH_4 separation in a wide range of temperatures (Fig. 4E and fig. S39C). We measured membrane stability under thermal stress, and the (001)-AlFFIVE/6FDA-DAM-DAT membrane demonstrated excellent reversibility in CO_2 permeability and CO_2/CH_4 selectivity in a wide range of temperatures and a duration of least 400 hours (Fig. 4F).

A comparison of CO_2/CH_4 separation performance of [001]-oriented membranes with other reported MOF-nanoparticle/6FDA-polyimide membranes is presented in Fig. 4G and tables S13 to S15. It is clear from Fig. 4G that the performance of the [001]-oriented membranes reported here exceeds that of others reported in the literature. More appropriate comparison with MOF-nanosheet/polymer membranes attests to the superior performance of [001]-oriented membranes (fig. S40 and table S14) (17, 18, 34, 35). The CO_2/CH_4 separation on ultrathin [001]-oriented membrane on porous α-Al$_2$O$_3$ supports was assessed. Preliminary results exhibited an 11-fold increase of CO_2 permeance compared with thick membranes, and selectivity was preserved (fig. S41). Although better separation performances have been reported for thin supported zeolite and carbon molecular sieve membrane films (36), this family of MMMOF membranes have a straightforward manufacture process, excellent mechanical properties, and stability for streaming, and no signs of plasticization were observed for more than 30 days.

Because CO_2/CH_4 separation at relatively low CO_2 concentrations (10%) is more challenging than at high concentrations (50%), the latter is typically used for study purposes (table S15). The [001]-oriented membranes

demonstrated outstanding separation at relatively low CO_2 concentration. Therefore, we dedicated our gas separation to the ternary mixture under realistic raw natural gas composition ($H_2S/CO_2/CH_4$: 1/9/90; 2/18/80 and 5/5/90) (37). For natural gas purification, both CO_2 and H_2S must be removed from CH_4, so the acid gas removal performance can be evaluated by measuring the total acid gas permeability [$P(CO_2) + P(H_2S)$] and selectivity [$P(CO_2) + P(H_2S)$]/$P(CH_4)$] (11). Even under an $H_2S/CO_2/CH_4$:1/9/90 mixture, the mixed-gas ($H_2S + CO_2$) permeability improvement of 63, 104, and 140%, and the (H_2S+CO_2)/CH_4 selectivity enhancement of 123, 112, and 103% were achieved for the (001)-AlFFIVE(58.9)/6FDA-DAM, (001)-AlFFIVE(59.6)/6FDA-DAM-DAT, and (001)-AlFFIVE(60.3)/6FDA-DAT membranes, respectively, compared with the associated pure polymer membranes (table S16). AlFFIVE-1-Ni has a similar adsorption selectivity (H_2S/CO_2 selectivity close to 1), so it is capable of removing both gases simultaneously (26). We have demonstrated an adsorbent separation selectivity that can be translated into the processable matrix.

The comparative study reveals that the performance of the [001]-oriented membranes reported here exceeds that of others reported in the literature (Fig. 4H) (11, 38, 39). The performance stability of membrane under continuously mixed-gas permeation conditions is a critical test to assess the membrane longevity and the reproducibility of its associated properties. Direct application of our best-performing membranes to a feed 1/9/90:H_2S/CO_2/CH_4 mixture led to 6/85/09:$H_2S/CO_2/CH_4$ mixture in the permeate side for at least 30 days of continuous operation (fig. S42).

We further evaluated the separation performance of [001]-oriented membranes under high-feed pressure that reflects practical natural gas purification (40). Membrane permeation was studied under high-feed pressures up to 35 bar (Fig. 4I and fig. S43). No abrupt selectivity and/or permeability loss occurred in the [001]-oriented membranes for the total acid gas removal, even under 35 bar pressure (figs. S43 and S44).

The separation performances of oriented membranes were further tested for other gas pairs, including H_2/N_2, H_2/CH_4, and H_2/C_3H_8, and subsequently compared with the literature (3) (fig. S45). The resultant membranes exhibited excellent selectivity and permeability enhancement for these gas pairs, far beyond the upper bounds for polymeric membranes.

Conclusions

The enhanced performances reported here can be rationalized by recognizing the importance of three essential criteria described earlier. The attainment of in-plane alignment and extremely high loading of (001) nanosheets is distinc-

tively responsible for the achieved separation performance. Nanosheets selectively transported gases based on their kinetic diameter through the oriented membranes. In fact, this centimeter-scale flexible [001]-oriented membrane can be regarded as a single piece of a flexible crystal in which thousands of nanosheets are uniformly aligned in a predefined crystallographic direction and the gaps between aligned nanosheets are filled with polymer. The results confirm the potential of tailoring MOF crystal morphology into oriented nanosheets, allowing the desired orientation of the 1D channels parallel to the gas diffusion direction and proffering opportunities to maximize the performance of the oriented membrane, as demonstrated here for various gas separations.

REFERENCES AND NOTES

1. Office of Scientific and Technical Information, US Department of Energy. "Materials for separation technologies: Energy and emission reduction opportunities" (OSTI, 2005); https://www.osti.gov/biblio/1218755.
2. D. S. Sholl, R. P. Lively, *Nature* **532**, 435–437 (2016).
3. L. M. Robeson, *J. Membr. Sci.* **320**, 390–400 (2008).
4. D. L. Gin, R. D. Noble, *Science* **332**, 674–676 (2011).
5. W. J. Koros, C. Zhang, *Nat. Mater.* **16**, 289–297 (2017).
6. J. Dechnik, J. Gascon, C. J. Doonan, C. Janiak, C. J. Sumby, *Angew. Chem. Int. Ed.* **56**, 9292–9310 (2017).
7. B. Seoane et al., *Chem. Soc. Rev.* **44**, 2421–2454 (2015).
8. G. Dong, H. Li, V. Chen, *J. Mater. Chem. A* **1**, 4610–4630 (2013).
9. Y. Cheng et al., *Adv. Mater.* **30**, e1802401 (2018).
10. J. Dechnik, C. J. Sumby, C. Janiak, *Cryst. Growth Des.* **17**, 4467–4488 (2017).
11. G. Liu et al., *Nat. Mater.* **17**, 283–289 (2018).
12. J. Sánchez-Laínez et al., *J. Membr. Sci.* **515**, 45–53 (2016).
13. A. Sabetghadam et al., *Adv. Funct. Mater.* **26**, 3154–3163 (2016).
14. B. Ghalei et al., *Nat. Energy* **2**, 17086 (2017).
15. A. Knebel et al., *Nat. Mater.* **19**, 1346–1353 (2020).
16. H. B. Park, J. Kamcev, L. M. Robeson, M. Elimelech, B. D. Freeman, *Science* **356**, eaab0530 (2017).
17. T. Rodenas et al., *Nat. Mater.* **14**, 48–55 (2015).
18. A. Pustovarenko et al., *Adv. Mater.* **30**, e1707234 (2018).
19. X. Li, J. Hou, R. Guo, Z. Wang, J. Zhang, *ACS Appl. Mater. Interfaces* **11**, 24618–24626 (2019).
20. Y. Cheng et al., *ACS Appl. Mater. Interfaces* **10**, 43095–43103 (2018).
21. C. Li, C. Wu, B. Zhang, *ACS Sustain. Chem. Eng.* **8**, 642–648 (2019).
22. O. Kwon et al., *Sci. Adv.* **8**, eabl6841 (2022).
23. P. M. Bhatt, V. Guillerm, S. J. Datta, A. Shkurenko, M. Eddaoudi, *Chem* **6**, 1613–1633 (2020).
24. Y. Li, Z. Fu, G. Xu, *Coord. Chem. Rev.* **388**, 79–106 (2019).
25. A. Cadiau et al., *Science* **356**, 731–735 (2017).
26. Y. Belmabkhout et al., *Nat. Energy* **3**, 1059–1066 (2018).
27. M. Zhao et al., *Chem. Soc. Rev.* **47**, 6267–6295 (2018).
28. L. Zhuang et al., *Angew. Chem. Int. Ed.* **58**, 13565–13572 (2019).
29. S. Zhao et al., *Nat. Energy* **1**, 16184 (2016).
30. C. Zhao et al., *Nature* **580**, 210–215 (2020).
31. C. J. Brinker, Y. Lu, A. Sellinger, H. Fan, *Adv. Mater.* **11**, 579–585 (1999).
32. Y. Zhu et al., *Adv. Mater.* **32**, e1907941 (2020).
33. J. G. Wijmans, R. W. Baker, *J. Membr. Sci.* **107**, 1–21 (1995).
34. Y. Yang, K. Goh, R. Wang, T. H. Bae, *Chem. Commun. (Camb).* **53**, 4254–4257 (2017).
35. M. Shete et al., *J. Membr. Sci.* **549**, 312–320 (2018).
36. D. D. Iarikov, S. T. Oyama, in *Membrane Science and Technology*, S. T. Oyama, S. M. Stagg-Williams, Eds. (Elsevier, 2011), vol. 14, pp. 91–115.
37. M. A. Al-Saleh, S. O. Duffuaa, M. A. Al-Marhoun, J. A. Al-Zayer, *Energy* **16**, 1089–1099 (1991).

38. G. Liu *et al.*, *Angew. Chem. Int. Ed.* **57**, 14811–14816 (2018).
39. M. Z. Ahmad *et al.*, *Separ. Purif. Tech.* **230**, 115858 (2020).
40. R. W. Baker, K. Lokhandwala, *Ind. Eng. Chem. Res.* **47**, 2109–2121 (2008).

SUPPLEMENTARY MATERIALS

science.org/doi/10.1126/science.abe0192
Materials and Methods
Supplementary Text
Figs. S1 to S47
Tables S1 to S20
References (*41–99*)
Movies S1 and S2